

Sweep data of electrical impedance tomography

Harri Hakula, Lauri Harhanen and Nuutti Hyvönen

Department of Mathematics and Systems Analysis, Aalto University, P.O.Box 11100,
FI-00076 Aalto, Finland

E-mail: harri.hakula@tkk.fi, lauri.harhanen@tkk.fi,
nuutti.hyvonen@hut.fi

Abstract. This work considers electrical impedance tomography in the special case that the boundary measurements of current and voltage are carried out with two (infinitely) small electrodes. One of the electrodes lies at a fixed position while the other is moved along the object boundary in a sweeping motion, with the corresponding measurement being the (relative) potential difference required for maintaining a unit current between the two electrodes. Assuming that the two-dimensional object of interest has constant background conductivity but is contaminated by compactly supported inhomogeneities, it is shown that such sweep data represents the boundary value of a holomorphic function defined in the exterior of the embedded inclusions. This observation makes it possible to use the sweep data as the input for the convex source support method in order to localize conductivity inhomogeneities. The functionality of the resulting algorithm is demonstrated by numerical experiments both with idealized point electrode data and with simulated complete electrode model measurements.

AMS classification scheme numbers: 35R30, 65N21

Submitted to: *Inverse Problems*

1. Introduction

Electrical impedance tomography (EIT) is a noninvasive imaging technique for recovering information about the conductivity distribution inside a physical body from boundary measurements of current and voltage. It has applications, e.g., in medical imaging, process tomography, and nondestructive testing of materials; see the review articles [1, 3, 26] and the references therein. In this work we consider EIT in the special case that the boundary measurements are carried out with only two electrodes.

Throughout this text our two-dimensional object of interest is assumed to have constant isotropic background conductivity with a compactly supported (possibly anisotropic) embedded inhomogeneity. We consider the following measurement setting: One of the two electrodes lies at a fixed position while the other moves along the object boundary in a sweeping motion. One unit of current is maintained between the electrodes and the corresponding voltage difference is recorded as a function of the location of the dynamic electrode. We call the alteration in such measurement caused by the inhomogeneity the *sweep data* of EIT. The objective of this work is to extract information on the whereabouts of the conductivity inhomogeneity from the sweep data. (Notice that the needed reference measurement corresponding to a homogeneous object can in practice be computed if the constant background conductivity is known, and sometimes, e.g., in the case of time difference imaging, it may also be measured with the same equipment as the data for the inhomogeneous body.)

In the theoretical part of this text, we adopt the so-called *point electrode model* (PEM), i.e., we model the electrodes as unit point current sources (cf., e.g., [5]), which is a good approximation if the used electrodes are small; in our setting the discrepancy between the PEM and the *complete electrode model* (CEM) [4, 23] is of the order $O(d^2)$ where $d > 0$ is the length of the electrodes [9, Theorem 2.1]. Following the ideas in [13] for the backscatter data of EIT (see also [8, 12, 15]), we show that the sweep data can be continued as a holomorphic function to the exterior of the conductivity inhomogeneity. With the help of such an extension, it is then demonstrated that the sweep data can be used as the input for the convex source support method [11], resulting in the concept of *convex sweep support* and an algorithm for reconstructing it; see [20] for the original ideas behind this technique. In particular, the convex sweep support is a nonempty subset of the convex hull of the support of the conductivity inhomogeneity, assuming that the sweep data is nonconstant. The functionality of the ensuing inclusion detection algorithm is tested with numerical experiments, some of which are based on simulated CEM data.

Although the ideas and techniques utilized in this work resemble to a certain extent the ones in [13], there are also some essential differences. Most importantly, the backscatter data considered in [13] is realized by conducting a single dipole current, not two point currents of opposite signs like here, through the object boundary, and then taking the tangential derivative of the corresponding relative boundary potential. Such a measurement can be emulated in practice up to the order $O(d)$ by letting a net

current of $1/(2d)$ units flow between two electrodes of length $d > 0$ at distance d from each other, and then dividing the (relative) potential difference between the electrodes by d [9, Theorem 4.1]. In order to obtain a good approximation of the backscatter data, one thus needs to apply high net currents, which is naturally suspect in real-life, and/or to divide the resulting voltage measurements by a small number, which is bound to amplify the noise content of the (relative) backscatter data (cf. [9, Section 4]). These practical complications can be explained in an intuitive manner as follows: If the used small electrodes lie close to each other, the voltage measurements do not carry legible information about the conductivity distribution far away from the boundary as most electrons travel between the two electrodes without ever visiting the interior of the object. For the sweep data promoted in this work, these kinds of difficulties are not as severe because the two electrodes do not move together along the object boundary, and thus there are reasonable current densities in the interior of the object even without application of unrealistically high net currents through the electrodes. Compared to the material in [13], we also present three other enhancements, namely the theoretical treatment of anisotropic conductivity inhomogeneities, the formulation of the results for general smooth, bounded and simply connected domains, not just for the unit disk as in [13], and the testing of the reconstruction algorithm with simulated CEM data.

This text is organized as follows. In Section 2, we list our assumptions and recall a couple of useful tools from [13]. Section 3 introduces the sweep data and proves some of its basic properties. In Section 4 it is shown that the sweep data can be continued as a holomorphic function to the exterior of the conductivity inhomogeneity. Subsequently, the convex sweep support is defined in Section 5 and the algorithm for reconstructing it is outlined in Section 6. Finally, Section 7 presents the numerical examples and Section 8 lists the concluding remarks.

2. Assumptions and background material

Let $D \subset \mathbb{R}^2$ be a simply connected and bounded domain with a C^∞ -boundary. Assume that the symmetric conductivity $\sigma \in L^\infty(D, \mathbb{R}^{2 \times 2})$ satisfies the conditions

$$\sigma \geq cI \quad \text{for } c > 0 \quad \text{and} \quad \text{supp}(\sigma - I) \quad \text{is a compact subset of } D,$$

where $I \in \mathbb{R}^{2 \times 2}$ is the identity matrix and the first condition is to be understood in the sense of positive definiteness. We fix $\Sigma \subset D$, consisting of finitely many simply connected, nonempty, closed and mutually disjoint sets Σ_j , $j = 1, \dots, m$, such that

$$\text{supp}(\sigma - I) \subset \Sigma \subset D. \tag{2.1}$$

(Take note that here we choose Σ to be closed, not open as in [13].) In addition, for technical reasons which will become apparent in what follows, we introduce simply connected C^∞ -domains Ω_j , $j = 1, \dots, m$, such that $\Sigma_j \subset \Omega_j$, $\overline{\Omega}_j \subset D$ and $\overline{\Omega}_j \cap \overline{\Omega}_k = \emptyset$ for $j \neq k$. The union of these domains is denoted by Ω .

Let us consider the boundary value problem

$$\nabla \cdot (\sigma \nabla u) = 0 \quad \text{in } D, \quad \frac{\partial u}{\partial \nu} = f \quad \text{on } \partial D, \tag{2.2}$$

where ν is the exterior unit normal of ∂D . According to the material in, e.g., [13, Appendix], for any boundary current density f in

$$H_\diamond^s(\partial D) = \{g \in H^s(\partial D) \mid \langle g, 1 \rangle_{\partial D} = 0\}, \quad s \in \mathbb{R}, \quad (2.3)$$

the problem (2.2) has a unique solution u in $(H^{\min\{1, s+3/2\}}(D) \cap H_{\text{loc}}^1(D))/\mathbb{C}$, where

$$H_{\text{loc}}^1(D) = \{v \in \mathcal{D}'(D) \mid \varphi v \in H^1(D) \text{ for every } \varphi \in C_0^\infty(D)\}.$$

Here and in what follows, $\langle \cdot, \cdot \rangle_{\partial D} : H^s(\partial D) \times H^{-s}(\partial D) \rightarrow \mathbb{C}$ denotes the dual evaluation between Sobolev spaces on ∂D ; if there is no possibility for a mix-up we refrain from marking the spaces in the brackets and use this same notation for the induced duality between $H_\diamond^s(\partial D)$ and $H^{-s}(\partial D)/\mathbb{C}$. Moreover, unless there is room for confusion, we identify an equivalence class of a quotient Sobolev space with any representative of the class in question.

The Neumann-to-Dirichlet map

$$\Lambda : f \mapsto u|_{\partial D}, \quad H_\diamond^s(\partial D) \rightarrow H^{s+1}(\partial D)/\mathbb{C}, \quad (2.4)$$

is well defined and bounded for every $s \in \mathbb{R}$ (cf., e.g., [13, Appendix]). The same also applies to the reference Neumann-to-Dirichlet map

$$\Lambda_0 : f \mapsto u_0|_{\partial D}, \quad H_\diamond^s(\partial D) \rightarrow H^{s+1}(\partial D)/\mathbb{C},$$

where $u_0 \in H^{s+3/2}(D)/\mathbb{C}$ is the unique solution of (see [21, Chapter 2, Remark 7.2])

$$\Delta u_0 = 0 \quad \text{in } D, \quad \frac{\partial u_0}{\partial \nu} = f \quad \text{on } \partial D. \quad (2.5)$$

Because σ is identically I in some (interior) neighborhood of ∂D , it follows that $u - u_0$ is smooth near the boundary ∂D , and the relative Neumann-to-Dirichlet map

$$\Lambda - \Lambda_0 : H_\diamond^{-s}(\partial D) \rightarrow H^s(\partial D)/\mathbb{C} \quad (2.6)$$

is bounded for any fixed $s \in \mathbb{R}$ (cf., e.g., [13, Appendix]).

To be able to prove some useful properties of the sweep data of EIT that is introduced in the following section, we need to recall a factorization of the difference boundary map $\Lambda - \Lambda_0$ from [13]. To this end, we first introduce the space

$$H^s(\partial\Omega)/\mathbb{C}^m := (H^s(\partial\Omega_1)/\mathbb{C}) \oplus \dots \oplus (H^s(\partial\Omega_m)/\mathbb{C}), \quad s \in \mathbb{R},$$

and note that its dual is realized by

$$H_\diamond^{-s}(\partial\Omega) := H_\diamond^{-s}(\partial\Omega_1) \oplus \dots \oplus H_\diamond^{-s}(\partial\Omega_m),$$

where the components are defined in accordance with (2.3). Let us then introduce the linear and bounded operator

$$T : f \mapsto u_0|_{\partial\Omega}, \quad H_\diamond^s(\partial D) \rightarrow H^{1/2}(\partial\Omega)/\mathbb{C}^m, \quad (2.7)$$

where u_0 is the unique solution of (2.5) and thus smooth in the interior of Ω (cf., e.g., [21, Chapter 2, Remark 7.2 and Theorem 3.2]). It is important to note that although the Dirichlet trace of u_0 on $\partial\Omega$ is defined up to only one additive constant, i.e., up to the ground level of potential, here we interpret $u_0|_{\partial\Omega}$ as an element of $H^{1/2}(\partial\Omega)/\mathbb{C}^m$

by letting each component $u_0|_{\partial\Omega_j}$, $j = 1, \dots, m$, float independently, that is, we let each $u_0|_{\partial\Omega_j}$ define an equivalence class in the corresponding component quotient space $H^{1/2}(\partial\Omega_j)/\mathbb{C}$.

With these tools in hand, we are ready to restate [13, Corollary 3.2]. The proof is omitted as it is in essence the same as that of [13, Corollary 3.2], although here we consider a slightly more general framework allowing anisotropic conductivities; see, e.g., [6, 18] for other factorizations of $\Lambda - \Lambda_0$ in the anisotropic setting.

Theorem 2.1. *The operator $\Lambda - \Lambda_0$ can be factored as*

$$\Lambda - \Lambda_0 = T^*GT, \quad (2.8)$$

where $G : H^{1/2}(\partial\Omega)/\mathbb{C}^m \rightarrow H_{\infty}^{-1/2}(\partial\Omega)$ is a bounded linear operator, which coincides with its own dual. Moreover, G can be extended to a continuous operator from $H^s(\partial\Omega)/\mathbb{C}^m$ to $H_{\infty}^{-s}(\partial\Omega)$ for any $s \in \mathbb{R}$.

As the intermediate operator G is well defined on $H^{1/2}(\partial\Omega)/\mathbb{C}^m$, it does not see additions of constants to the components of its argument (cf. [13, Remark 3]). To make this statement more concrete, let $\psi = \bigoplus_{j=1}^m \psi_j$ be any element of $H^{1/2}(\partial\Omega) = \bigoplus_{j=1}^m H^{1/2}(\partial\Omega_j)$, introduce an arbitrary constant vector $c \in \mathbb{C}^m$, and set $\psi + c = \bigoplus_{j=1}^m (\psi_j + c_j)$. Then, it holds that $G(\psi + c) = G\psi$ since $\psi + c = \psi$ in the topology of $H^{1/2}(\partial\Omega)/\mathbb{C}^m$. This property of G will be essential in the analysis of Section 4 below.

3. Sweep data of EIT

Let us then consider a specific localized current pattern, namely $\delta_y - \delta_{y_0} \in H_{\diamond}^{-1/2-\epsilon}(\partial D)$, $\epsilon > 0$, with $y, y_0 \in \partial D$ and δ_z denoting the delta distribution located at z on ∂D . Due to the boundedness of the boundary operator (2.6) and since $\delta_y - \delta_{y_0}$ has zero mean in the sense of (2.3), the quantity

$$\varsigma(y) = \langle (\Lambda - \Lambda_0)(\delta_y - \delta_{y_0}), (\delta_y - \delta_{y_0}) \rangle_{\partial D} \quad (3.1)$$

is well defined. The function $\varsigma : \partial D \rightarrow \mathbb{R}$ is what we call the sweep data of EIT. According to [9], such data can be approximated in practice as follows: Unit current is maintained between two small (but finite) electrodes at y_0 and y while the latter is moved along ∂D in a sweeping motion. The corresponding potential difference between the electrodes is recorded as a function of y , and the actual sweep-type data is finally obtained by subtracting the corresponding measurement in the case that $\sigma \equiv 1$. In the framework of the CEM [4, 23], the discrepancy between such a realistic data set and ς is of the order $O(d^2)$, where $d > 0$ is the length of the used electrodes; see [9, Theorem 2.1] for the details.

Remark 3.1. *The sweep data can alternatively be given in the form*

$$\varsigma(y) = (u^y - u_0^y)(y) - (u^y - u_0^y)(y_0), \quad (3.2)$$

where u^y and u_0^y are the solutions of (2.2) and (2.5), respectively, for $f = \delta_y - \delta_{y_0}$. In particular, the alteration of $y \in \partial D$ affects not only the argument of the first term on the right-hand side of (3.2) but also the involved potentials u^y and u_0^y via the applied current pattern. This means that the sweep measurement is considerably different from a standard (idealized) EIT measurement pair, which consists of an applied boundary current density and the resulting potential measured everywhere on the object boundary. On the other hand, the sweep data does resemble the backscatter data of EIT [12, 13] to a certain extent.

According to the Riemann mapping theorem, there exists a conformal map Φ that sends D onto the unit disk B and y_0 to $z_0 = (1, 0) \in \partial B$. As D has a smooth boundary, Φ also defines a smooth diffeomorphism of ∂D onto ∂B [22, Section 3.3]. We denote the inverse of Φ by Ψ , and let $\tilde{\Lambda}$ be the Neumann-to-Dirichlet map corresponding to B and the conductivity

$$\tilde{\sigma} = J_\Psi^{-1}(\sigma \circ \Psi)(J_\Psi^{-1})^T \det J_\Psi \in L^\infty(B, \mathbb{R}^{2 \times 2}), \quad (3.3)$$

where J_Ψ denotes the Jacobian of Ψ . Take note that $\tilde{\sigma}$ is a feasible conductivity in the sense of Section 2, i.e.,

$$\sigma \geq \tilde{c}I \quad \text{for } \tilde{c} > 0 \quad \text{and} \quad \text{supp}(\tilde{\sigma} - I) \quad \text{is a compact subset of } B,$$

because $\Psi : \bar{B} \rightarrow \bar{D}$ is a diffeomorphism and as a conformal mapping it satisfies

$$J_\Psi^T J_\Psi = (\det J_\Psi)I. \quad (3.4)$$

In particular, $\tilde{\sigma} = \sigma \circ \Psi$ for an isotropic σ . We let $\tilde{\Lambda}_0$ be the Neumann-to-Dirichlet map corresponding to B and the unit conductivity. The (pushforward) sweep data $\tilde{\zeta} : \partial B \rightarrow \mathbb{R}$ corresponding to the unit disk B and the conductivity $\tilde{\sigma}$ is defined in the natural way, i.e.,

$$\tilde{\zeta}(z_\theta) = \langle (\tilde{\Lambda} - \tilde{\Lambda}_0)(\delta_{z_\theta} - \delta_{z_0}), (\delta_{z_\theta} - \delta_{z_0}) \rangle_{\partial B}, \quad (3.5)$$

where the bracket denotes the Sobolev duality on ∂B and $z_\theta = (\cos \theta, \sin \theta)$ for some polar angle $\theta \in \mathbb{R}$. The following theorem demonstrates that Φ can be used to transfer sweep data between ∂D and ∂B .

Theorem 3.2. *It holds that*

$$\varsigma = \tilde{\zeta} \circ \Phi,$$

where $\varsigma : \partial D \rightarrow \mathbb{R}$ and $\tilde{\zeta} : \partial B \rightarrow \mathbb{R}$ are the sweep data defined by (3.1) and (3.5), respectively.

Proof. Let us fix $y \in \partial D$ and denote by $\tilde{u} \in (H^{1-\epsilon}(B) \cap H_{\text{loc}}^1(B))/\mathbb{C}$, $\epsilon > 0$, the unique solution of the Neumann problem

$$\nabla \cdot (\tilde{\sigma} \nabla \tilde{u}) = 0 \quad \text{in } B, \quad \frac{\partial \tilde{u}}{\partial \nu} = \delta_{\Phi(y)} - \delta_{z_0} \quad \text{on } \partial B. \quad (3.6)$$

Our initial aim is to show that $u = \tilde{u} \circ \Phi$ satisfies (2.2) for $f = \delta_y - \delta_{y_0}$. Take note that $u \in (H^{1-\epsilon}(D) \cap H_{\text{loc}}^1(D))/\mathbb{C}$ because Φ and Ψ are diffeomorphisms with bounded derivatives up to an arbitrary order (cf., e.g., [21, 22]).

We start by tackling the first equation of (2.2). Let $\varphi \in C_0^\infty(D)$ be arbitrary. Since $u \in H_{\text{loc}}^1(D)$ and $\tilde{u} \in H_{\text{loc}}^1(B)$, using an obvious change of variables we may write

$$\begin{aligned} \int_D \sigma \nabla u \cdot \nabla \varphi \, dx &= \int_D \sigma J_\Phi^T(\nabla \tilde{u} \circ \Phi) \cdot \nabla \varphi \, dx \\ &= \int_B (\sigma \circ \Psi)(J_\Phi^T \circ \Psi) \nabla \tilde{u} \cdot (\nabla \varphi \circ \Psi) \det J_\Psi \, dx \\ &= \int_B (\sigma \circ \Psi)(J_\Psi^{-1})^T \nabla \tilde{u} \cdot (J_\Psi^{-1})^T \nabla(\varphi \circ \Psi) \det J_\Psi \, dx \\ &= \int_B \tilde{\sigma} \nabla \tilde{u} \cdot \nabla \tilde{\varphi} \, dx \end{aligned}$$

for $\tilde{\varphi} = \varphi \circ \Psi \in C_0^\infty(B)$ due to the definition of $\tilde{\sigma}$. Since \tilde{u} satisfies the first equation of (3.6), it thus follows from the definition of distributional differentiation that

$$\int_D \sigma \nabla u \cdot \nabla \varphi \, dx = 0$$

for any $\varphi \in C_0^\infty(D)$, which in turn is just the weak form of the first equation of (2.2).

Next we show that u satisfies the boundary condition of (2.2) with $f = \delta_y - \delta_{y_0}$. Let $\varphi \in C^\infty(\partial D)$ be arbitrary and extend it as a smooth function to D so that (cf., e.g., [21, Chapter 1, Theorem 9.4])

$$\frac{\partial \varphi}{\partial \nu} = 0 \quad \text{on } \partial D \quad \text{and} \quad \text{supp } \varphi \subset \overline{D} \setminus \Sigma.$$

Now it follows from the generalized Green's formula [21, Chapter 2, Theorem 6.5 with $r = 0$] that

$$\left\langle \frac{\partial u}{\partial \nu}, \varphi \right\rangle_{\partial D} = - \int_D u \Delta \varphi \, dx = - \int_D (\tilde{u} \circ \Phi) \Delta \varphi \, dx.$$

A change of variables thus yields

$$\left\langle \frac{\partial u}{\partial \nu}, \varphi \right\rangle_{\partial D} = - \int_B \tilde{u} ((\Delta \varphi) \circ \Psi) \det J_\Psi \, dx = - \int_B \tilde{u} \Delta \tilde{\varphi} \, dx,$$

where $\tilde{\varphi} = \varphi \circ \Psi$ and the second step is a straightforward consequence of the fact that Ψ satisfies the Cauchy–Riemann equations. As conformal mappings retain homogeneous Neumann boundary conditions, we see that

$$\frac{\partial \tilde{\varphi}}{\partial \nu} = 0 \quad \text{on } \partial B \quad \text{and} \quad \text{supp } \tilde{\varphi} \subset \overline{B} \setminus \Phi(\Sigma).$$

Because $\text{supp}(\tilde{\sigma} - I) \subset \Phi(\Sigma)$ due to (2.1) and (3.4), we can use the generalized Green's formula for a second time to come up with

$$\left\langle \frac{\partial u}{\partial \nu}, \varphi \right\rangle_{\partial D} = \left\langle \frac{\partial \tilde{u}}{\partial \nu}, \tilde{\varphi} \right\rangle_{\partial B} = \tilde{\varphi}(\Phi(y)) - \tilde{\varphi}(z_0) = \varphi(y) - \varphi(y_0),$$

where the second and third steps follow from the definitions of \tilde{u} and $\tilde{\varphi}$, respectively. Since the original $\varphi \in C^\infty(\partial D)$ was arbitrary, this means that

$$\frac{\partial u}{\partial \nu} = \delta_y - \delta_{y_0} \quad \text{on } \partial D,$$

and thus $u = \tilde{u} \circ \Phi$ is the unique solution of (2.2) for $f = \delta_y - \delta_{y_0}$.

A simplified version of the above line of reasoning shows that the solution of (2.5) for $f = \delta_y - \delta_{y_0}$ can be given as $u_0 = \tilde{u}_0 \circ \Phi$, where $\tilde{u}_0 \in H^{1-\epsilon}(B)/\mathbb{C}$ is the unique solution of (3.6) when $\tilde{\sigma}$ is replaced by I . In consequence, we have

$$\begin{aligned} \varsigma(y) &= \langle (\Lambda - \Lambda_0)(\delta_y - \delta_{y_0}), (\delta_y - \delta_{y_0}) \rangle_{\partial D} \\ &= (u - u_0)(y) - (u - u_0)(y_0) \\ &= (\tilde{u} - \tilde{u}_0)(\Phi(y)) - (\tilde{u} - \tilde{u}_0)(\Phi(y_0)) \\ &= \langle (\tilde{\Lambda} - \tilde{\Lambda}_0)(\delta_{\Phi(y)} - \delta_{z_0}), (\delta_{\Phi(y)} - \delta_{z_0}) \rangle_{\partial B} = \tilde{\zeta}(\Phi(y)). \end{aligned}$$

Because $y \in \partial D$ was chosen arbitrarily, this completes the proof. \square

4. Analytic continuation of the sweep data

In this section, we will follow the argumentation of [13] for the case of the backscatter data to establish that the sweep data ς is the boundary value of a univalent holomorphic function defined in the exterior of Σ ; note that if the topology of $\text{supp}(\sigma - I)$ is not very complicated, we can choose Σ to be the so-called infinity support of $\sigma - I$, which is, in essence, composed of $\text{supp}(\sigma - I)$ together with the holes in it [20]. Although the following analysis resembles that in [13], there is one essential difference: When the backscatter data is continued analytically to the exterior of the inhomogeneity in [13], the encountered singularities are poles located on the boundary of the inhomogeneity, or to be more precise on $\partial\Omega$. Here, we are forced to work with complex logarithms that have branch cuts extending from the origin to the boundary of Ω . In order to get rid of this hindrance, we must make explicit use the factor space property of G discussed after Theorem 2.1 to move the branch cuts entirely inside $\bar{\Omega}$. To begin with, we assume that D is the unit disk; this assumption will be relaxed at the end of this section with the help of Theorem 3.2.

Assume for the moment that $D = B$ is the unit disk. To begin with, we note that one representative of the equivalence class $T(\delta_{z_\theta} - \delta_{z_0}) \in H^{1/2}(\partial\Omega)/\mathbb{C}^m$ is given by (see, e.g., [13, Section 4] or [14, Appendix])

$$\tilde{g}_\theta(x) := \frac{1}{\pi}(\log|x - z_0| - \log|x - z_\theta|), \quad x \in \partial\Omega.$$

As a consequence, Theorem 2.1 allows us to write the sweep data introduced in Section 2 in the form

$$\varsigma(z_\theta) = \langle GT(\delta_{z_\theta} - \delta_{z_0}), T(\delta_{z_\theta} - \delta_{z_0}) \rangle_{\partial\Omega} = \int_{\partial\Omega} (G\tilde{g}_\theta)(x) \tilde{g}_\theta(x) \, ds(x), \quad (4.1)$$

where the second equality is a consequence of the regularity properties of G . Let us then fix points $y^{(k)} \in \Sigma_k$, $k = 1, \dots, m$, and make the componentwise definition

$$g_\theta(x) := \tilde{g}_\theta(x) + \frac{1}{2\pi}(\log|z_\theta - y^{(k)}| + i(\phi_k - \theta)), \quad x \in \partial\Omega_k, \quad k = 1, \dots, m,$$

where $\phi_k = \phi_k(\theta)$ is the polar angle of the point $z_\theta - y^{(k)}$, i.e., the polar angle of z_θ with respect to $y^{(k)}$, defined in such a way that the mapping $\mathbb{R} \ni \theta \mapsto \phi_k(\theta) - \theta$ is continuous, 2π -periodic and takes values in the open interval $(-\pi/2, \pi/2)$; a simple geometric considerations shows that such a choice is possible. Obviously, g_θ and \tilde{g}_θ belong to the same equivalence class of $H^{1/2}(\partial\Omega)/\mathbb{C}^m$, and thus we have

$$\varsigma(z_\theta) = \int_{\partial\Omega} (Gg_\theta)(x) g_\theta(x) ds(x) = \sum_{j=1}^m \int_{\partial\Omega_j} (Gg_\theta)(x) g_\theta(x) ds(x),$$

which holds for all polar angles $\theta \in \mathbb{R}$.

Let us then introduce the complex variables $\xi = \xi(x) = x_1 + ix_2$, $\zeta = e^{i\theta}$ and $v_k = y_1^{(k)} + iy_2^{(k)}$, $k = 1, \dots, m$, and identify D with the unit disk of the complex plane when appropriate. By slight abuse of the notation, we obtain for $x \in \partial\Omega_k$ that

$$\begin{aligned} g_\theta(x) &= \frac{1}{2\pi} \log \left(\frac{|1 - \xi|^2 \zeta - v_k}{|\zeta - \xi|^2 \zeta} \right) \\ &= \frac{1}{2\pi} \log \left(\frac{|1 - \xi|^2 \zeta - v_k}{1 - \bar{\xi}\zeta \zeta - \xi} \right) \\ &= \frac{1}{2\pi} \left(\log \frac{|1 - \xi|^2}{1 - \bar{\xi}\zeta} + \log \frac{\zeta - v_k}{\zeta - \xi} \right) =: g_k(x, \zeta), \end{aligned} \quad (4.2)$$

where at every occurrence \log denotes the principal value of the complex logarithm. Indeed, the first equality of (4.2) holds due to the definition of ϕ_k , and the second one follows from a trivial algebraic manipulation. To see that the third equality of (4.2) is also valid, notice first that the argument of $|1 - \xi|^2/(1 - \bar{\xi}\zeta)$ is in the interval $(-\pi/2, \pi/2)$ — modulo 2π — because the real part of this expression is positive for all $x \in \partial\Omega_k$ and $\zeta \in \partial D$. Moreover, it follows from a straightforward geometric reasoning that the argument of $(\zeta - v_k)/(\zeta - \xi)$ is in the open interval $(-\pi, \pi)$ — modulo 2π — for all $x \in \partial\Omega_k$ and $\zeta \in \partial D$. To sum up, for any fixed $x \in \partial\Omega_k$ and $\zeta \in \partial D$ the second and third lines of (4.2) represent logarithms of the same complex number, with the corresponding imaginary parts in $(-\pi/2, \pi/2)$ and $(-3\pi/2, 3\pi/2)$, respectively. As different branches of the complex logarithm differ by integer multiples of $2\pi i$, we thus deduce that the expressions on the second and third lines of (4.2) must, in fact, be the same, i.e., $g_\theta(x) = g_k(x, \zeta)$ for all $x \in \partial\Omega_k$ and $\zeta = e^{i\theta} \in \partial D$.

It is obvious that g_k can be extended as a continuous function to $\partial\Omega_k \times (\bar{D} \setminus \bar{\Omega}_k)$, with the first variable treated as a point in \mathbb{R}^2 and the second as an element of \mathbb{C} : For any fixed $\xi = \xi(x) \in \partial\Omega_k \subset \mathbb{C}$, the first term of $g_k(x, \cdot)$ can be chosen to have a branch cut from $\zeta = 1/\bar{\xi} \notin \bar{D}$ to infinity without intersecting D , and the second term a branch cut from $\zeta = \xi$ to $\zeta = v_k$ within $\bar{\Omega}_k$. Moreover, this extended g_k is complex differentiable with respect to $\zeta \in D \setminus \bar{\Omega}_k$, with the corresponding derivative also being a continuous function in $\partial\Omega_k \times (\bar{D} \setminus \bar{\Omega}_k)$, as apparent from the explicit representation

$$\partial_\zeta g_k(x, \zeta) = \frac{1}{2\pi} \left(\frac{\bar{\xi}}{1 - \bar{\xi}\zeta} + \frac{1}{\zeta - v_k} - \frac{1}{\zeta - \xi} \right).$$

(Notice that if this same technique had been applied directly to the original candidate \tilde{g}_θ , we would have ended up with $\tilde{g}_k(x, \cdot)$ having a branch cut between the origin and $\xi \in \partial\Omega_k$, since the second term on the last line of (4.2) would have been $\log(\zeta/(\zeta - \xi))$. In general, such \tilde{g}_k would not have been continuous in $\partial\Omega_k \times (\overline{D} \setminus \overline{\Omega}_k)$, and the reasoning presented below would not have been valid as such.)

We extend g_k as zero to $\cup_{j \neq k}(\partial\Omega_j \times \overline{D})$ continuing to denote it by the same symbol, which in particular means that

$$g_\theta(x) = \sum_{k=1}^m g_k(x, \zeta), \quad x \in \partial\Omega, \quad \zeta = e^{i\theta}.$$

Due to the linearity of G and through slight abuse of the notation, we thus see that

$$\varsigma(\zeta) = \sum_{j=1}^m \sum_{k=1}^m \int_{\partial\Omega_j} [Gg_k(\cdot, \zeta)](x) g_j(x, \zeta) ds(x), \quad \zeta \in \partial D.$$

It follows from the same line of reasoning as in [13, Lemma 4.1] that the function $[Gg_k(\cdot, \zeta)](x)$, $(x, \zeta) \in \partial\Omega \times (D \setminus \overline{\Omega}_k)$, is complex differentiable with respect to ζ . Moreover, both $[Gg_k(\cdot, \zeta)](x)$ and $\partial_\zeta [Gg_k(\cdot, \zeta)](x)$ are continuous in $\partial\Omega \times (\overline{D} \setminus \overline{\Omega}_k)$. As a consequence,

$$\varsigma_{jk}(\zeta) := \int_{\partial\Omega_j} [Gg_k(\cdot, \zeta)](x) g_j(x, \zeta) ds(x), \quad \zeta \in \partial D, \quad (4.3)$$

extends as a holomorphic function to $D \setminus (\overline{\Omega}_j \cup \overline{\Omega}_k)$ for all $1 \leq j, k \leq m$ due to the basic results on line integrals depending on a complex parameter (cf., e.g., [25, Proposition 27]). Altogether, we are ready to state the following.

Theorem 4.1. *Assume that D is the unit disk. Then, the sweep data ς of (3.1) extends as a holomorphic function to $D \setminus \Sigma$, with Σ as in Section 2.*

Proof. The same logic as in the proof of [13, Theorem 4.2] shows that ς_{jk} of (4.3) actually extends holomorphically to the whole domain $D \setminus (\Sigma_j \cup \Sigma_k) \supset D \setminus (\overline{\Omega}_j \cup \overline{\Omega}_k)$ for any $1 \leq j, k \leq m$. Hence,

$$\varsigma(\zeta) = \sum_{j=1}^m \sum_{k=1}^m \varsigma_{jk}(\zeta), \quad \zeta \in \partial D,$$

can be continued as a univalent holomorphic function to $D \setminus \cup_{j=1}^m \Sigma_j = D \setminus \Sigma$. \square

Corollary 4.2. *Assume that D is the unit disk. Then, the Cauchy problem*

$$\Delta v = 0 \quad \text{in } D \setminus \Sigma, \quad v = \varsigma \quad \text{on } \partial D, \quad \frac{\partial v}{\partial \nu} = 0 \quad \text{on } \partial D \quad (4.4)$$

has a solution.

Proof. The solution of (4.4) is given by the real part of the holomorphic extension of ς as reasoned in the proof of [13, Corollary 4.3] for the backscatter data of EIT. \square

We complete this section by noting that the statements of Theorem 4.1 and Corollary 4.2 remain valid for a general smooth and simply connected domain D . This generalization is a straightforward consequence of Theorem 3.2.

Theorem 4.3. *Theorem 4.1 and Corollary 4.2 remain valid for any simply connected and bounded C^∞ -domain $D \subset \mathbb{R}^2$.*

Proof. Assume that D is a simply connected and bounded C^∞ -domain, with the corresponding sweep data ς defined by (3.1). Furthermore, let B be the unit disk and Φ a conformal map sending D onto B and y_0 to $z_0 = (1, 0)$, with the inverse $\Psi = \Phi^{-1}$. As in Section 3, we denote the sweep data corresponding to B and the conductivity $\tilde{\sigma}$ of (3.3) by $\tilde{\zeta} : \partial B \rightarrow \mathbb{R}$. Since Φ is a diffeomorphism, the simply connected, nonempty and closed sets $\tilde{\Sigma}_j := \Phi(\Sigma_j)$, $j = 1, \dots, m$, satisfy $\tilde{\Sigma}_j \cap \tilde{\Sigma}_k = \emptyset$ for $j \neq k$. Moreover, due to (3.3) and (3.4), the union $\tilde{\Sigma} = \cup_{j=1}^m \tilde{\Sigma}_j$ has the property

$$\text{supp}(\tilde{\sigma} - I) \subset \tilde{\Sigma} \subset B.$$

According to Theorem 4.1 and Corollary 4.2, the modified sweep data $\tilde{\zeta}$ thus extends as a holomorphic function to $B \setminus \tilde{\Sigma}$, and the Cauchy problem

$$\Delta \tilde{v} = 0 \quad \text{in } B \setminus \tilde{\Sigma}, \quad \tilde{v} = \tilde{\zeta} \quad \text{on } \partial B, \quad \frac{\partial \tilde{v}}{\partial \nu} = 0 \quad \text{on } \partial B \quad (4.5)$$

has a solution.

Because $\varsigma = \tilde{\zeta} \circ \Phi$ due to Theorem 3.2, it is obvious that ς can be extended holomorphically from ∂D to $D \setminus \Psi(\tilde{\Sigma}) = D \setminus \Sigma$. Furthermore, if \tilde{v} is the solution of the Cauchy problem (4.5), then $\tilde{v} \circ \Phi$ is a solution of (4.4) since conformal mappings retain harmonicity and homogeneous Neumann boundary conditions. This completes the proof. \square

5. Convex sweep support

From the practical point of view, the most important observation of the preceding section was that the Cauchy problem for the Laplacian with the data $(\varsigma, 0)$ on ∂D attains a solution in the exterior of Σ , with Σ as in Section 2. As noted in the beginning of Section 4, if the topology of the set $\text{supp}(\sigma - I)$ is not very complicated, one can, loosely speaking, choose Σ to be $\text{supp}(\sigma - I)$ together with the holes in it, which would mean that the Cauchy data $(\varsigma, 0)$ can be continued harmonically up to the outer boundary of the conductivity inhomogeneity. Be that as it may, for the purposes of the analysis of the current section, it is enough to settle for a less optimal Σ , the existence of which is guaranteed by the following lemma. Here and in what follows, we denote the convex hull and the open ϵ -neighborhood of a set $A \subset \mathbb{R}^2$ by $\text{ch } A$ and $N_\epsilon(A)$, respectively.

Lemma 5.1. *There exists Σ satisfying the assumptions of Section 2 such that $\Sigma \subset D \cap \text{ch}(\text{supp}(\sigma - I))$.*

Proof. Due to an obvious compactness argument, the sets $\text{supp}(\sigma - I)$ and ∂D lie at a positive distance from each other. Hence, there exists a closed, injective curve that is composed of a finite number of line segments and is the boundary of a closed, simply connected set $\Sigma' \subset D$ such that $\text{supp}(\sigma - I) \subset \Sigma'$. Our aim is to prove that

$$\Sigma := \Sigma' \cap \text{ch}(\text{supp}(\sigma - I))$$

has the required properties. It is self-evident that Σ is closed and satisfies $\text{supp}(\sigma - I) \subset \Sigma \subset D$. In consequence, the only thing we need to show is that Σ is composed of a finite number of simply connected components.

To begin with, we note that either one of the trivial cases $\Sigma = \text{ch}(\text{supp}(\sigma - I))$ and $\Sigma = \Sigma'$ holds or the set Σ is composed of regions bounded partially by $\partial\Sigma'$ and partially by the boundary of $\Sigma'' := \text{ch}(\text{supp}(\sigma - I))$. In particular, Σ can have an infinite number of path connected components only if the (piecewise differentiable) curves $\partial\Sigma'$ and $\partial\Sigma''$ intersect an infinite number of times (with a common connected boundary section counted as a single intersection). Suppose that this is the case. Due to a compactness argument, say, $\partial\Sigma'$ must carry an accumulation point, any neighborhood of which contains an infinite number of intersections of the two boundary curves. However, since $\partial\Sigma'$ is composed of line segments of finite length and $\partial\Sigma''$ can be locally given as a graph of a convex function, it is obvious that such an accumulation point cannot exist. This is a contradiction, which shows that Σ is composed of a finite number of path connected components. To complete the proof, we note that every path connected component of $\Sigma = \Sigma' \cap \Sigma''$ is simply connected since the fundamental group of the intersection of any two simply connected planar sets is trivial (see, e.g., [17]). \square

Now we have gathered enough tools to introduce the convex sweep support and show that it carries some useful properties. To this end, let us consider the Poisson problem

$$\Delta w = F \quad \text{in } D, \quad \frac{\partial w}{\partial \nu} = 0 \quad \text{on } \partial D, \quad (5.1)$$

which has a unique solution $w \in \cup_{m \in \mathbb{Z}} H^m(D)/\mathbb{C}$ for any distributional source F in

$$\mathcal{E}'_{\diamond}(D) = \{v \in \mathcal{E}'(D) \mid \langle v, 1 \rangle_D = 0\},$$

where $\langle \cdot, \cdot \rangle_D : \mathcal{E}'(D) \times C^\infty(D) \rightarrow \mathbb{C}$ denotes the dual evaluation between compactly supported distributions and smooth functions in D (cf., e.g., [10, Section 2]). Since the solution w is smooth near the boundary ∂D (cf., e.g., [21]), the linear measurement operator

$$L : F \mapsto w|_{\partial D}, \quad \mathcal{E}'_{\diamond}(D) \rightarrow L^2(\partial D)/\mathbb{C},$$

is well defined.

Definition 5.2. Let $\text{supp}_c F$ be the convex hull of the support of $F \in \mathcal{E}'_{\diamond}(D)$. Then, the convex sweep support \mathcal{S}_{ζ} is defined to be

$$\mathcal{S}_{\zeta} = \bigcap_{LF=\zeta} \text{supp}_c F.$$

The convex sweep support \mathcal{S}_ζ is the convex source support corresponding to the boundary data ζ ; see [10, Definition 4.1] and [11, (2.1)]. In particular, \mathcal{S}_ζ need not be a subset of D , if D is nonconvex (cf. [11, Example 1]). On the positive side, the convex sweep support inherits useful properties from the convex source support, as concretized by the following theorem.

Theorem 5.3. *The convex sweep support \mathcal{S}_ζ is a subset of the convex hull of the inhomogeneity $\text{supp}(\sigma - I)$. Moreover, $\mathcal{S}_\zeta = \emptyset$ if and only if ζ is a constant, i.e., the zero element of $L^2(\partial D)/\mathbb{C}$.*

Proof. Although the assertion follows from the same ideas as [13, Theorem 5.2], we repeat the argumentation here since [13] only considers the case that D is convex, or more precisely the unit disk.

Let Σ satisfy the assumptions of Section 2 and be such that $\Sigma \subset D \cap \text{ch}(\text{supp}(\sigma - I))$; the existence of such a set is guaranteed by Lemma 5.1. We fix $\epsilon > 0$ so that $N_\epsilon(\Sigma)$ satisfies $\overline{N_\epsilon(\Sigma)} \subset D$ and consider the $L^2(D)$ -function

$$v_\epsilon = \begin{cases} v & \text{in } D \setminus N_\epsilon(\Sigma), \\ 0 & \text{otherwise,} \end{cases}$$

where v is the solution of the Cauchy problem (4.4) guaranteed by Theorem 4.3. It follows that $F_\epsilon = \Delta v_\epsilon \in \mathcal{E}'_\diamond(D) \cap H^{-2}(D)$ is supported in $\overline{N_\epsilon(\Sigma)}$ and, moreover,

$$LF_\epsilon = v_\epsilon|_{\partial D} = v|_{\partial D} = \zeta.$$

Since ϵ was chosen arbitrarily, we deduce that

$$\mathcal{S}_\zeta \subset \bigcap_{\epsilon > 0} \text{ch}(\overline{N_\epsilon(\Sigma)}) \subset \bigcap_{\epsilon > 0} \overline{N_\epsilon(\text{ch}(\text{supp}(\sigma - I)))} = \text{ch}(\text{supp}(\sigma - I)).$$

This proves the first part of the assertion. The second part follows from the properties of the convex source support established in [11, Theorem 2.1]. \square

6. Reconstruction algorithm

In this section, we will introduce an algorithm for reconstructing the convex sweep support \mathcal{S}_ζ in the case that the object of interest $D = B$ is the unit disk. This will also be the framework for our numerical studies in Section 7 below. However, Remark 6.1 at the end of this section considers two methods for generalizing our algorithm to the case of a general smooth, bounded and simply connected D . Because the reconstruction algorithm is essentially the same as the one presented in [11] for standard EIT data and subsequently in [13] for the backscatter data of EIT, we will skip many of the details and only outline the main ideas.

To begin with, we interpret ζ as a function of the polar angle and denote its Fourier coefficients by

$$\alpha_j = \frac{1}{2\pi} \int_{-\pi}^{\pi} \zeta(\theta) e^{-ij\theta} d\theta, \quad j \in \mathbb{Z}.$$

Moreover, we introduce the propagated sweep data via

$$\varsigma_\rho(\theta) = \sum_{j \in \mathbb{Z}} \frac{\alpha_j}{\rho^{|j|}} e^{ij\theta}, \quad \theta \in [-\pi, \pi), \quad (6.1)$$

for $\rho \geq 1$ (cf. [11, Lemma 3.1]).

Let us identify \mathbb{R}^2 with the complex plane, fix $\rho \geq 1$, and denote by B_ρ the open disk of radius ρ centered at the origin. Up to rotations of the image space all Möbius transformations mapping \overline{B}_ρ onto \overline{D} can be given as

$$\Phi_\zeta(z) = \rho \frac{z - \zeta}{\rho^2 - \overline{\zeta}z}, \quad (6.2)$$

where the free complex parameter $\zeta \in B_\rho$ determines the point that is mapped to the origin. We denote the inverse of Φ_ζ by Ψ_ζ , and the corresponding angular maps, sending $(-\pi, \pi]$ to itself, by

$$\varphi_\zeta : \theta \mapsto \arg \Phi_\zeta(\rho e^{i\theta}), \quad \psi_\zeta : \theta \mapsto \arg \Psi_\zeta(e^{i\theta}),$$

respectively. The Fourier coefficients of $\varsigma_\rho \circ \psi_\zeta$ are given by

$$\alpha_j(\zeta) = \frac{1}{2\pi} \int_{-\pi}^{\pi} \varsigma_\rho(\psi_\zeta(\theta)) e^{-ij\theta} d\theta = \frac{1}{2\pi} \int_{-\pi}^{\pi} \varsigma_\rho(\theta) e^{-ij\varphi_\zeta(\theta)} \varphi'_\zeta(\theta) d\theta, \quad j \in \mathbb{Z}. \quad (6.3)$$

With the help of these definitions, we have the following characterization (see [11, Corollary 3.3]): The convex sweep support \mathcal{S}_ζ is a subset of $\Psi_\zeta(\overline{B}_R)$, $0 \leq R < 1$, if and only if

$$\sum_{j \in \mathbb{Z}} \frac{|\alpha_j(\zeta)|^2}{(R + \epsilon)^{2|j|}} < \infty \quad (6.4)$$

for any $\epsilon > 0$.

In order to devise an algorithm based on this observation, we approximate the Fourier coefficients of the modified sweep data $\varsigma_\rho \circ \psi_\zeta$ by a logarithmic regression model

$$\log |\alpha_j(\zeta)| \approx a|j| + b, \quad a, b \in \mathbb{R}, \quad (6.5)$$

for $j \in \mathbb{Z}$, as suggested originally in [2]. Under the courtesy of the assumption that (6.5) is exact, inequality (6.4) asserts that the closed disk $\Psi_\zeta(\overline{B}_R)$ contains \mathcal{S}_ζ if and only if $R \geq R_\zeta := e^a$. This procedure can be carried out for a set of test points $\{\zeta_k\}$, producing a family of disks containing \mathcal{S}_ζ . We use the intersection of these disks as our approximation for the convex sweep support, i.e.,

$$\mathcal{S}_\zeta \approx \bigcap_k \Psi_{\zeta_k}(\overline{B}_{R_k}), \quad (6.6)$$

where we have used the short notation $R_k = R_{\zeta_k}$.

In all numerical tests presented in Section 7, we use the parameter value $\rho = 1.4$ and choose $\{\zeta_k\}$ to consist of 64 equidistant points on a circle of radius 0.7 around the origin. These are choices that have been found reasonable in [11, 13] for standard EIT data and backscatter data, respectively. Finally, it should be noted that the number of reliable Fourier coefficients for (6.5) varies with ζ and the amount of model and measurement noise in the data (cf. Section 7): For low spatial frequencies the logarithms of $|\alpha_j(\zeta)|$

lie approximately on a descending line as functions of $|j|$, while the high frequency coefficients consist of noise. In consequence, an adaptive method must be devised to pick a cut-off frequency for determining the coefficients to be used in (6.5). There are a number of reasonable ways for making such a choice. In this work we resort to the most fundamental one and use visual inspection.

Remark 6.1. *There are two ways to use the above introduced algorithm for gathering information about the conductivity inhomogeneity in the case that D is not the open unit disk, but only a smooth, bounded and simply connected domain.*

First of all, if a conformal map Φ sending D onto the open unit disk B is known, one can use Theorem 3.2 to obtain the sweep data $\tilde{\zeta}$ corresponding to B and the pushforward conductivity $\tilde{\sigma}$ given by (3.3). Subsequently, the convex sweep support corresponding to $\tilde{\sigma}$ and B , say $\mathcal{S}\tilde{\zeta}$, can be reconstructed by our algorithm and mapped by $\Psi = \Phi^{-1}$ back inside D . Since $\mathcal{S}\tilde{\zeta}$ lies within the convex hull of $\text{supp}(\tilde{\sigma} - I) = \Phi(\text{supp}(\sigma - I))$, the obtained set $\Psi(\mathcal{S}\tilde{\zeta})$ carries information about the whereabouts of the original inhomogeneity $\text{supp}(\sigma - I)$. However, $\Psi(\mathcal{S}\tilde{\zeta})$ is not, in general, the original convex sweep support $\mathcal{S}\zeta$.

In order to introduce the second option, we note that \overline{D} may be assumed to lie inside B ; if this was not the case, we could resort to scaling and translation. Let us consider $\varsigma \in L^2(\partial D)/\mathbb{C}$ as the Dirichlet data of the solution to the Poisson problem (5.1) with an unspecified source F , and then compute the Dirichlet data, say $g \in L^2(\partial B)/\mathbb{C}$, of the solution to the Poisson problem with the very same source but with D replaced by B in (5.1). This can be done by solving a suitable transmission problem without any further knowledge about F ; see [11, Section 2.1] for the details. After this, one can use the above outlined algorithm to approximate the convex source support $\mathcal{C}g$ corresponding to g ; see [11] where the algorithm was originally introduced for the purpose of reconstructing convex source supports. It follows from [11, Theorem 2.3] that $\mathcal{C}g$ is always contained within $\mathcal{S}\zeta$ and empty if and only if $\mathcal{S}\zeta$ is empty. Moreover, if D is convex, then $\mathcal{C}g$ is exactly $\mathcal{S}\zeta$.

7. Numerical experiments

In this section we test our reconstruction algorithm in the case that the object of interest D is the open unit disk; see Remark 6.1 and the numerical test of [7] for treatment of more general domains. Our numerical experiments consider the conductivity inhomogeneities depicted in Figure 1: A kite-shaped inclusion with isotropic constant conductivity $\sigma = 2$ on the left, a disk and a square with isotropic constant conductivities $\sigma = 2$ and $\sigma = 0.5$, respectively, on the right. The conductivity levels of these inclusions are held fixed throughout the numerical studies, and the static electrode location is chosen to be $y_0 = (1, 0)$ if not stated otherwise. We employ three data sets of varying quality: They are called *ideal*, *realistic* and *noisy realistic* as explained in what follows.

To obtain *ideal data*, the relative boundary potential $(\Lambda - \Lambda_0)(\delta_y - \delta_{y_0}) \in C^\infty(\partial D)/\mathbb{C}$ is simulated with the help of layer potential techniques for all y belonging to an

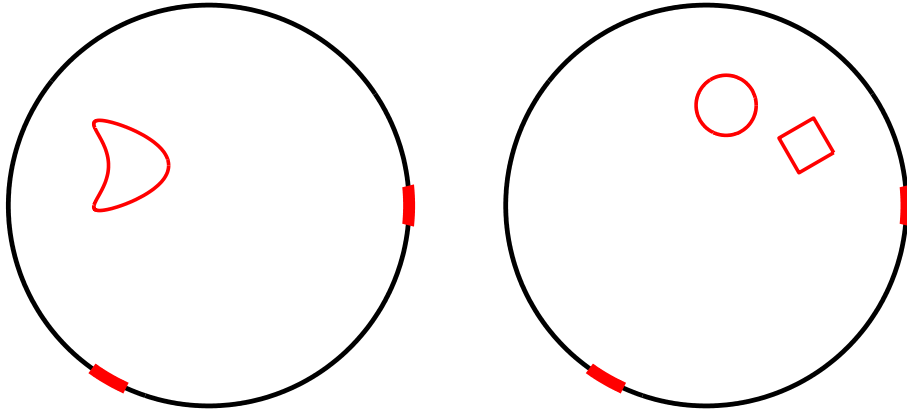


Figure 1. The studied inclusions in comparison with the unit disk and the two CEM electrodes of length $d = \pi/16$ used for gathering the CEM sweep data. Left: Kite-shaped inhomogeneity with constant isotropic conductivity 2. Right: Discoidal and square inhomogeneities with constant isotropic conductivities 2 and 0.5, respectively.

equidistant grid of 1000 points on ∂D (cf., e.g., [12, Example 2.2], [14, Appendix] and [19]). Subsequently, the sweep data

$$\varsigma(y) = \left((\Lambda - \Lambda_0)(\delta_y - \delta_{y_0}) \right)(y) - \left((\Lambda - \Lambda_0)(\delta_y - \delta_{y_0}) \right)(y_0)$$

is evaluated at every point y of the very same grid. These 1000 point values of ς are then used as the input for the algorithm introduced in Section 6; see [11] for the technical details of the numerical implementation. The sweep data simulated in this manner is very accurate, and thus the corresponding reconstructions should reflect the limits for the functionality of the proposed algorithm.

To simulate realistic measurements, we resort to the CEM [4, 23]. We denote by e_y an electrode of length $0 < d < \pi$ around $y = (\cos \theta, \sin \theta) \in \partial D$, i.e.,

$$e_y = \{(\cos \phi, \sin \phi) \in \partial D \mid |\phi - \theta| < d/2\}.$$

Moreover, we let $z > 0$ be the contact resistance, which is a characteristic of real-life electrode measurements. For a given conductivity distribution σ that is feasible in the sense of Section 2, the potential pair $(u^y, U^y) \in H^1(D) \oplus \mathbb{R}$ is defined as the unique solution of [23]

$$\begin{aligned} \nabla \cdot (\sigma \nabla u^y) &= 0 && \text{in } D, \\ \frac{\partial u^y}{\partial \nu} &= 0 && \text{on } \partial D \setminus (\bar{e}_y \cup \bar{e}_{y_0}), \\ u^y + z \frac{\partial u^y}{\partial \nu} &= U^y && \text{on } e_y, \\ u^y + z \frac{\partial u^y}{\partial \nu} &= -U^y && \text{on } e_{y_0}, \\ \int_{e_y} \frac{\partial u^y}{\partial \nu} ds &= 1, && \int_{e_{y_0}} \frac{\partial u^y}{\partial \nu} ds = -1, \end{aligned} \tag{7.1}$$

where we have assumed that $e_y \cap e_{y_0} = \emptyset$ and chosen the ground level of potential so that the two electrodes are at opposite voltages. We denote the reference potentials,

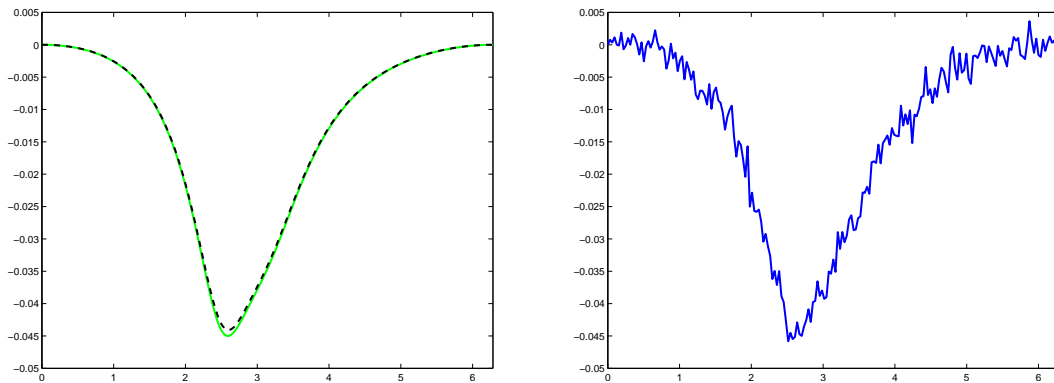


Figure 2. Comparison of the three data types as functions of the polar angle of y for $y_0 = (1, 0)$ and the inclusion geometry in the left-hand image of Figure 1. Left: ideal data (solid) and realistic data (dashed). Right: noisy realistic data.

i.e., the solution of (7.1) for $\sigma \equiv 1$, by $(u_0^y, U_0^y) \in H^1(D) \oplus \mathbb{R}$. In real life, noisy versions of the electrode potentials U^y and U_0^y can be obtained through electrode measurements carried out with two electrodes [4, 23]. With this in mind, we define the *CEM sweep measurement* at $y \in \partial D$, with $e_y \cap e_{y_0} = \emptyset$, as

$$\varsigma_d(y) = \left(U^y - (-U^y) \right) - \left(U_0^y - (-U_0^y) \right) = 2(U^y - U_0^y), \quad (7.2)$$

i.e., as the change in the potential difference between the two electrodes caused by the conductivity inhomogeneity. This notion is reasonable because

$$|\varsigma(y) - \varsigma_d(y)| \leq Cd^2 \quad (7.3)$$

for $y \in \partial D$ such that $e_y \cap e_{y_0} = \emptyset$, according to [9, Theorem 2.1].

With these tools in hand, *realistic data* are constructed as follows: We simulate the point values of ς_d , with $z = 0.1$ and $d = \pi/16 \approx 0.20$ (cf. Figure 1), on the grid $y^{(j)} = (\cos(2\pi j/J), \sin(2\pi j/J))$, $j = 1, \dots, J = 200$, by solving (7.1) and the corresponding reference problem by *hp*-FEM (cf., e.g., [16, 24]) for $y = y^{(j)}$, $j = 1, \dots, J$. To be quite precise, depending on the chosen static electrode location y_0 some grid values of ς_d are not defined by (7.2) due to overlapping of the electrodes in (7.1). We take care of this problem in the natural way by setting $\varsigma_d(y_0) = \varsigma(y_0) = 0$ and using linear interpolation to estimate the other missing values of ς_d . The *noisy realistic data* are then formed by adding a realization of a normally distributed random variable with zero mean and standard deviation $0.001|U^{y^{(j)}}|$ to $\varsigma_d(y^{(j)})$ for each $j = 1, \dots, J$. Loosely speaking, this means that the noise content of the electrode measurement is assumed to be 0.1 per cent. The reader should note, however, that this procedure results in a far higher noise content in the point values of the (relative) CEM sweep data ς_d because the ratio $|U^y|/|\varsigma_d(y)|$ is over 40 for any $y \in \partial D$ in all of our numerical examples. The different data types are compared in Figure 2 for the kite-shaped inclusion of conductivity $\sigma = 2$ shown in the left-hand image of Figure 1.

Remark 7.1. *If the measurement noise manifests itself in the absolute electrode measurement, as we have assumed in the simulation of the noisy realistic data set above,*

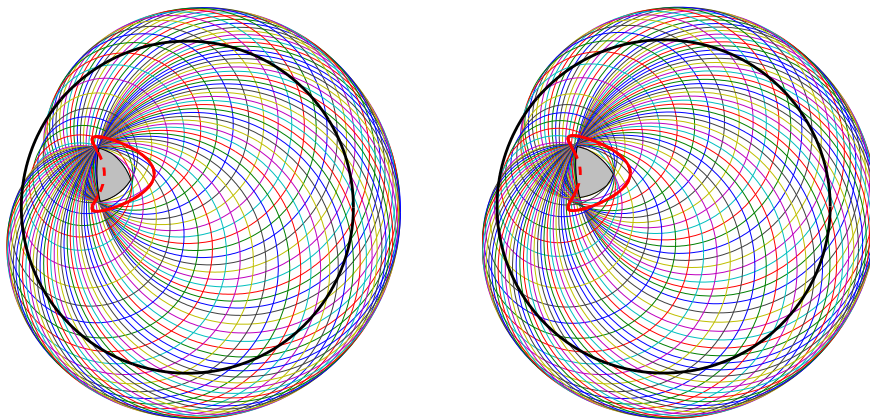


Figure 3. Reconstructions corresponding to ideal data and the left-hand inclusion geometry of Figure 1. The unit disk and the inhomogeneity are drawn by thick line, while the thin circles correspond to the disks in the intersection on the right-hand side of (6.6). The reconstructions are coloured with grey. Left: $y_0 = (1, 0)$. Right: $y_0 = (-1, 0)$.

it is not necessarily a good idea to use as small electrodes as possible when measuring sweep data in practice: According to (7.1), the absolute value of the mean current density through the two electrodes is $1/d$. In consequence, due to the Robin boundary conditions on the electrodes, the absolute value of the electrode potential U^y , and thus also the ratio $|U^y|/|\zeta_d(y)|$, gets larger as the electrodes get smaller. If the amount of measurement noise is proportional to $|U^y|$, as it is assumed to be in our model, the measurement noise content of the CEM sweep data thus increases as the electrode size decreases — under the assumption that the contact resistance z is not affected by the electrode size. To sum up, decreasing the size of the electrodes cuts down the model error (cf. (7.3)) but increases the noise content of the electrode sweep data.

In the first numerical experiment we work with ideal data and the left-hand inclusion geometry of Figure 1. The aim is to test how the location of the static electrode affects the functionality of our algorithm: The left-hand image of Figure 3 shows the obtained reconstruction for $y_0 = (1, 0)$ and the right-hand image the one for $y_0 = (-1, 0)$. Here and in all the other visualized reconstructions, the unit disk D and the inhomogeneity are plotted with thick line, while the thin circles depict the boundaries of the disks entering on the right-hand side of (6.6), with their intersection being the reconstruction of the convex sweep support. For both choices of y_0 , the reconstruction looks approximately like the convex hull of a smaller kite-shaped region. In particular, the algorithm seems to provide information on both the location and the shape of the inhomogeneity. As the position of the static electrode does not seem to play a major role, we fix it to be $y_0 = (1, 0)$ for the rest of this text.

The second test continues to consider ideal data, but this time the inclusions in the right-hand image of Figure 1 move into the focus of our attention. The left-hand reconstruction of Figure 4 corresponds to the case that merely the square inhomogeneity

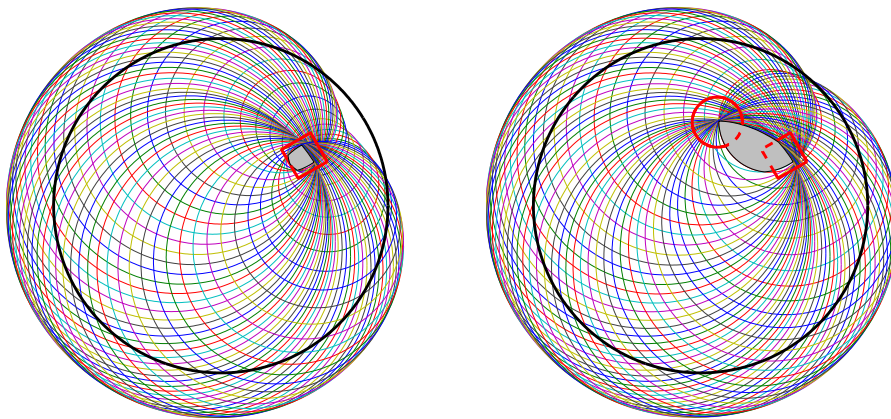


Figure 4. Reconstructions corresponding to ideal data and the two inclusions in the right-hand image of Figure 1. The unit disk and the inhomogeneities are drawn by thick line, while the thin circles correspond to the disks in the intersection on the right-hand side of (6.6). The reconstructions are coloured with grey. Left: the square inclusion. Right: the combination of the disk and the square.

contaminates D , whereas the right-hand image visualizes the performance of our algorithm with both the square and the discoidal inclusion inside the unit disk. For the square inhomogeneity the reconstruction is approximately a smaller square. This is, actually, how the algorithm typically functions for any convex polygonal inhomogeneity of constant conductivity: The corresponding reconstruction is (almost) a polygon of similar shape but smaller size. The observed discrepancy in size could be fixed by omitting some lowest frequencies j in the linear regression model (6.5): According to our experience, only the approximate location of the polygonal inclusion is visible in the Fourier coefficients corresponding to low spatial frequencies whereas high-frequency coefficients contain information about the corners. However, this would not be a very practical solution because the high-frequency information is unattainable in real-life due to measurement and model noise. On the other hand, the reconstruction corresponding to the combination of the disk and the square extends over both inclusions, indicating clearly their location. In fact, the estimated convex sweep support in the right-hand image of Figure 4 is a rounder version of the convex hull of the corresponding reconstructions computed separately for each of the two inclusions. (The reconstruction for the square is already shown in the left-hand image of Figure 4, while the one corresponding to the mere discoidal inhomogeneity is just one point approximately at the center of the respective inclusion; see [13] for similar results for disk-like inhomogeneities in the framework of backscattering.)

In the third and final numerical example, we consider realistic and noisy realistic data; the images in the left-hand column of Figure 5 correspond to the former and those in the right-hand column to the latter. The top row of Figure 5 represents reconstructions for the kite-shaped inclusion depicted in the left-hand image of Figure 1. For (exact) realistic data the obtained reconstruction is also kite-shaped but significantly smaller than the original inclusion, whereas the reconstruction corresponding to

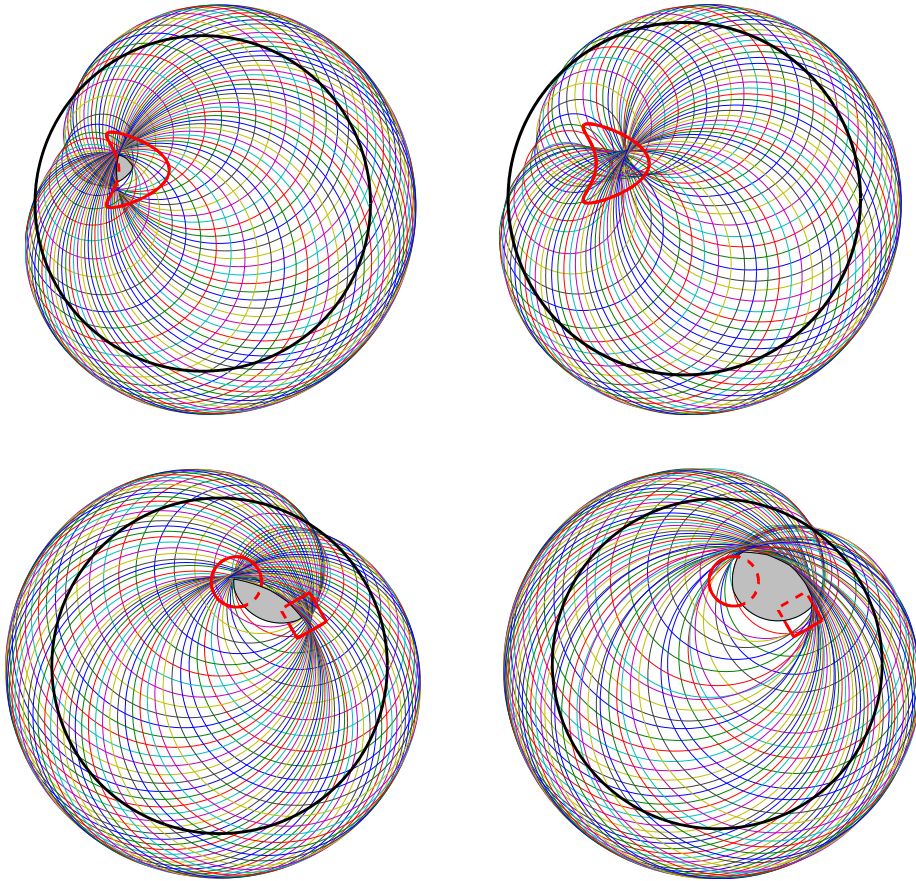


Figure 5. Reconstructions corresponding to realistic and noisy realistic data sets. The unit disk and the inhomogeneities are drawn by thick line, while the thin circles correspond to the disks in the intersection on the right-hand side of (6.6). The reconstructions are coloured with grey. Left column: realistic data. Right column: noisy realistic data. Top row: the kite-shaped inclusion. Bottom row: the combination of the disk and square inclusions.

noisy realistic data is empty but the region through which all the thin circles pass clearly indicates the approximate location of the conductivity inhomogeneity. The images in the bottom row of Figure 5 correspond to the the combination of the two inhomogeneities depicted in the right-hand image of Figure 1. For this inclusion geometry, the reconstruction provided by our algorithm is nonempty and extends over both components of the inhomogeneity for both realistic and noisy realistic data, with the one corresponding to the noiseless measurement being in a better agreement with the ideal reconstruction in the right-hand image of Figure 4.

To sum up, the proposed algorithm provides information about the location of the conductivity inhomogeneity for all three data types. However, only the reconstructions corresponding to ideal data contain any clear information about the shape of the searched for inclusions. Our results for ideal data are slightly worse than the ones presented in [13] for the idealized backscatter measurement, but we anticipate that this inferiority is overshadowed by the practicality of the sweep measurement promoted in

this work.

8. Concluding remarks

We have introduced the sweep data of EIT, which can be approximated by real-life measurements performed with two small electrodes, and shown that it can be used as the input for the convex source support method [11] in order to reconstruct the so-called convex sweep support. The functionality of the resulting numerical inclusion detection algorithm was demonstrated both with idealized PEM and realistic CEM data.

Acknowledgments

The work of L. Harhanen and N. Hyvönen was supported by the Finnish Graduate School in Computational Sciences FICS, the Finnish Funding Agency for Technology and Innovation TEKES (contract 40370/08) and the Academy of Finland (the Centre of Excellence in Inverse Problems Research and projects 115013 and 135979).

References

- [1] Borcea L 2002 Electrical impedance tomography *Inverse Problems* **18** R99–136
- [2] Brühl M and Hanke M 2000 Numerical implementation of two noniterative methods for locating inclusions by impedance tomography *Inverse Problems* **16** 1029–42
- [3] Cheney M, Isaacson D and Newell J C 1999 Electrical impedance tomography *SIAM Rev.* **41** 85–101
- [4] Cheng K-S, Isaacson D, Newell J S and Gisser D G 1989 Electrode models for electric current computed tomography *IEEE Trans. Biomed. Eng.* **36** 918–24
- [5] Delbary F and Kress R 2010 Electrical impedance tomography with point sources *Jour. Integral Equations Appl.* **22** 193–216
- [6] Gebauer B 2006 The factorization method for real elliptic problems *Z. Anal. Anwend.* **25** 81–102
- [7] Hakula H and Hyvönen N 2008 Two noniterative algorithms for locating inclusions using one electrode measurement of electric impedance tomography *Inverse Problems* **24** 055018 (16pp)
- [8] Hanke M 2011 Locating several small inclusions in impedance tomography from backscatter data *Submitted*
- [9] Hanke M, Harrach B and Hyvönen N 2011 Justification of point electrode models in electrical impedance tomography *Math. Models Methods Appl. Sci.* accepted.
- [10] Hanke M, Hyvönen N, Lehn M and Reusswig S 2008 Source supports in electrostatics *BIT* **48** 245–64
- [11] Hanke M, Hyvönen N and Reusswig S 2008 Convex source support and its application to electric impedance tomography *SIAM J. Imag. Sci.* **1** 364–78
- [12] Hanke M, Hyvönen N and Reusswig S 2010 An inverse backscatter problem for electric impedance tomography *SIAM J. Math. Anal.* **41** 1948–66
- [13] Hanke M, Hyvönen N and Reusswig S 2011 Convex backscattering support in electric impedance tomography *Numer. Math.* **117** 373–96
- [14] Harhanen L and Hyvönen N 2010 Convex source support in half-plane *Inverse Probl. Imaging* **4** 429–48
- [15] Hollborn S 2011 Reconstructions from backscatter data in electric impedance tomography *Submitted*

- [16] Hyvönen N, Hakula H and Pursiainen S 2007 Numerical implementation of the factorization method within the complete electrode model of electrical impedance tomography *Inverse Probl. Imaging* **1** 299-317
- [17] Karimov U H, Repovš D and Željko M 2005 On unions and intersections of simply connected planar sets *Monatsh. Math.* **145** 239-45
- [18] Kirsch A 2005 The factorization method for a class of inverse elliptic problems *Math. Nachr.* **278** 258-77
- [19] Kress R 1999 *Linear Integral Equations* 2 ed (New York: Springer-Verlag)
- [20] Kusiak S and Sylvester J 2003 The scattering support *Comm. Pure Appl. Math.* **56** 1525-48
- [21] Lions J L and Magenes E 1972 *Non-Homogeneous Boundary Value Problems and Applications* vol I (Berlin: Springer-Verlag)
- [22] Pommerenke Ch 1992 *Boundary Behaviour of Conformal Maps* (Berlin: Springer-Verlag)
- [23] Somersalo E, Cheney M and Isaacson D 1992 Existence and uniqueness for electrode models for electric current computed tomography *SIAM J. Appl. Math.* **52** 1023-40
- [24] Szabo B and Babuska 1991 *Finite Element Analysis* (New York: John Wiley & Sons)
- [25] Tutschke W and Vasudeva H L 2005 *An Introduction to Complex Analysis: Classical and Modern Approaches* (Boca Raton: Chapman & Hall)
- [26] Uhlmann G 2009 Electrical impedance tomography and Calderón's problem *Inverse Problems* **25** 123011